

Bio-synthesized TiO₂ nanoparticles and the aqueous binder-based anode derived thereof for lithium-ion cells

Akhilash Mohanan Pillai^{1,2} · Sumol V. Gopinadh¹ · Peddinti V. R. L. Phanendra¹ · Patteth S. Salini¹ · Bibin John¹ · Sujatha SarojiniAmma¹ · Mercy Thelakkattu Devassy³

Received: 29 December 2023 / Accepted: 9 April 2024

Published online: 17 April 2024

© The Author(s) 2024 [OPEN](#)

Abstract

Titanium dioxide nanoparticles (TiO₂-NPs) are a promising anode material for Lithium-ion batteries (LIBs) due to their good rate capability, low cost, non-toxicity, excellent structural stability, extended cycle life, and low volumetric change (~4%) during the Li⁺ insertion/de-insertion process. In the present paper, anatase TiO₂-NPs with an average particle size of ~12 nm were synthesized via a green synthesis route using Beta vulgaris (Beetroot) extract, and the synthesized TiO₂-NPs were evaluated as anode material in LIBs. Furthermore, we employed an aqueous binder (1:1 mixture of carboxy methyl cellulose and styrene butadiene) for electrode processing, making the process cost-effective and environmentally friendly. The results revealed that the Li/TiO₂ half-cells delivered an initial discharge capacity of 209.7 mAh g⁻¹ and exhibited superior rate capability (149 mAh g⁻¹ at 20 C) and cycling performances. Even at the 5C rate, the material retained a capacity of 82.2% at the end of 100 cycles. The synthesis route of TiO₂-NPs and the aqueous binder-based electrode processing described in the present work are facile, green, and low-cost and are thus practically beneficial for producing low-cost and high-performance anodes for advanced LIBs.

Keywords Lithium-ion batteries · Green-synthesis · TiO₂-NPs · Water-based binder · Electrochemical performance

1 Introduction

Lithium-ion batteries (LIBs) conquered the burgeoning global electric vehicle (EV) market due to their high power and energy densities and extended cycle life [1–7]. A typical LIB is composed of a cathode, anode, electrolyte, and separator. Current commercial LIBs employ LiCoO₂ (LCO), LiMn₂O₄ (LMO), LiFePO₄ (LFP), LiNi_{1/3}Mn_{1/3}Co_{1/3}O₂ (NMC 111), or LiNi_{0.8}Mn_{0.1}Co_{0.1}O₂ (NMC 811) as cathode materials, and graphite or carbonaceous materials as anode materials [8–14]. Among the various components, anode materials play a pivotal role in determining the electrochemical performance of LIBs. The widely used graphitic carbon anode suffers from several thorny issues, which hinder their commercial applications in high-power LIBs. These problems include expansion and shrinkage of graphite during the lithium-ion insertion and de-insertion process, which causes graphite particles to crack, leading to increased self-discharge or safety issues [15]. Thus researchers investigated many alternative anode-active materials, which would circumvent these limitations. As an alternative to graphitic carbon, several materials like CuO, NiO, SnO₂, Co₃O₄, fiberlike-Fe₂O₃, Li₄Ti₅O₁₂, Si, anatase-TiO₂, rutile-TiO₂, etc. have been explored [16, 17]. Among these, active materials such as Si, NiO, SnO₂, CuO, and Fe₂O₃ suffer

✉ Bibin John, bbnjohn@yahoo.com | ¹Energy Systems Development Division, Energy Systems Group, PCM Entity, Vikram Sarabhai Space Centre, Thiruvananthapuram, Kerala 695022, India. ²University of Kerala, Thiruvananthapuram 695034, India. ³Energy Systems Group, PCM Entity, Vikram Sarabhai Space Centre, Thiruvananthapuram, Kerala 695022, India.



from high volume expansion and structural deformation, which leads to capacity fading. In contrast, metal oxides such as $\text{Li}_4\text{Ti}_5\text{O}_{12}$, CeO_2 , and TiO_2 exhibit relatively smaller volume expansion during the charging/discharging process [18–20].

Among the various metal oxide anode materials, TiO_2 is considered as a promising anode candidate for LIBs, owing to its non-toxicity, low cost, high capacity, excellent structural stability, extended cycle life, and relatively small volume change (~4%) during Li^+ insertion/de-insertion process [21, 22]. Moreover, another intriguing aspect of TiO_2 is that it has a greater operating potential than graphite anode (> 1.5 V vs Li^+/Li), which could effectively inhibit the formation of lithium dendrites and lithium plating [23, 24]. TiO_2 exists in various polymorphic forms such as brookite (space group: Pbc_a), anatase (space group: I41/amd), rutile (space group: P42/mnm), ramsdellite (space group: Pbnm), and bronze TiO_2 -B (space group: C2/m) [25, 26]. During the insertion-deinsertion reaction, the anatase framework can accommodate 0.5 Li per formula unit with excellent insertion kinetics, whereas brookite and rutile lattices can accommodate only a small percentage of lithium ions. It is known that reducing the particle size from micron to nanoscale increases the surface area of the electrode–electrolyte interface, shortens the ion and electron paths, and thus leads to improved specific capacity and rate capability. Various synthesis strategies including sol–gel, hydrothermal, evaporation-induced self-assembly (EISA), electrospinning, etc. are employed to synthesize TiO_2 nanoparticles (TiO_2 -NPs) [26–28]. However, these processes are intricate, energy-intensive, and challenging for mass production [29, 30]. On the contrary green synthesis has been widely endorsed, as it is devoid of the toxic effects of various chemical methods. Thus, to reduce complexity and increase process efficiency, we have adopted an easy, inexpensive, and environmentally friendly bio-synthetic approach for the synthesis of TiO_2 -NPs.

In the present work, TiO_2 -NPs have been synthesized by a green-mediated approach using *Beta vulgaris* (Beetroot) extract. Bio-molecules present in the extract act as both reducing agents as well as capping agents and are thus responsible for the formation of TiO_2 -NPs. The present bio-mediated process minimizes complexity and makes the process cost-effective. The biosynthesized TiO_2 -NPs were well characterized and investigated its electrochemical performance as anode material for LIB application. Moreover, in this work, we employed a water-based binder (a combination of carboxymethyl cellulose (CMC) and styrene butadiene rubber (SBR)) for electrode processing, which strongly reduces the inconveniences caused by commonly employed PVDF binder which requires toxic and costly solvents like 1-methyl-2-pyrrolidinone (NMP) for processing [31]. Hence, the present manuscript highlights a completely green approach for the synthesis as well as the electrode processing of TiO_2 -NPs.

2 Materials and methods

2.1 Reagents

Titanium isopropoxide purchased from Sigma Aldrich was used as such without further purification. Beetroot (*Beta vulgaris*) was obtained from the local market in Mangad, Kollam, Kerala.

2.2 Extract preparation

Beta vulgaris (beetroot) was thoroughly washed with distilled water before being cut into pieces. 10 g of beetroot was boiled in 100 mL of double-deionized water for 15 min to get the extract. For the synthesis of TiO_2 -NPs, the resultant extract was cooled, filtered, and placed in a refrigerator.

2.3 Synthesis of TiO_2 -NPs

In the field of nanotechnology, the green synthesis of nanomaterials from plants or plant component extracts has received much attention. Green-mediated nanoparticles synthesis utilizes a bottom-up approach in which synthesis occurs with the help of reducing and stabilizing agents. Physical and chemical methods usually require toxic chemicals as capping agents to maintain stability, thus leading to toxicity in the environment. Currently, researchers are employing green nanoparticle synthesis as a simple, cost-effective, non-toxic, and environment-friendly technique for the synthesis of a variety of materials. The plant extracts rich in phytochemicals can act as both reducing agent and capping or stabilization agent.

In the present study, TiO₂-NPs were synthesized as follows: 80 ml of 0.5 M titanium isopropoxide solution in isopropyl alcohol was added to 80 ml of beetroot extract (v/v = 1:1) and stirred at 50–60 °C for 3 h. The obtained precipitate was thoroughly washed, filtered, and dried and was heated in a furnace at 500 °C for 5 h to remove the organic components. The obtained TiO₂-NPs were thoroughly characterized.

2.4 Material characterization

X-ray diffraction (XRD, Cu K α radiation ($\lambda = 0.15406$ nm), Bruker D8 Discover) was employed to characterize the crystalline structure of TiO₂-NPs over 2 θ range from 10° to 80°. The crystallite size was calculated by the Debye–Scherrer equation. Scanning electron microscopy (FE-SEM, GEMINI SEM 500) was used to analyze the morphology of the prepared TiO₂-NPs. High-resolution transmission electron microscopy (HR-TEM) and selected area electron diffraction (SAED) were used to investigate the structure of the as-prepared sample. FTIR (Nicolet i550 FTIR) spectra were recorded to examine the characteristic functional groups. LabRAM HR Evol spectrometer was used to record Raman scattering (RS) spectra. Using the Brunauer–Emmett–Teller (BET) method, the surface area and pore volume were determined.

2.5 Electrochemical measurements

TiO₂-NPs, acetylene black, CMC, and SBR were mixed in the weight ratio 80:10:5:5 with de-ionized water to prepare a slurry. The obtained slurry was then coated on a copper foil and then dried under vacuum at 70 °C and calendered; then the circular discs were punched out with a diameter of 12 mm. The electrode had a mass loading of about 2.3 mg cm⁻². Standard two-electrode CR2032-type coin cells were used to evaluate the electrochemical performance. Metallic lithium acts as both the reference and counter electrode in electrochemical measurement. The half-cell was assembled in an argon-filled glove box with a Celgard 2320 membrane as the separator, and 1 M LiPF₆ in a mixture of ethylene carbonate (EC), diethyl carbonate (DEC), and ethyl methyl carbonate (EMC) (1:1:1, by weight) as the electrolyte. Using a NEWARE battery tester, charge/discharge cycling tests were carried out at room temperature in the constant current-constant voltage (CC-CV) mode in the voltage window of 1.0–3.0 V vs Li⁺/Li. To investigate the redox characteristics, cyclic voltammetry (CV) was carried out at a scan rate of 100 μVs^{-1} in the voltage window of 0.5 to 3.5 V. CV measurements were also carried out at various scan rates (100 μVs^{-1} to 900 μVs^{-1}) to evaluate the diffusion coefficient of TiO₂-NPs based anode.

3 Results and discussions

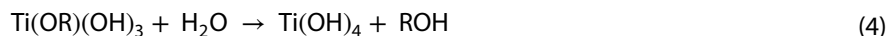
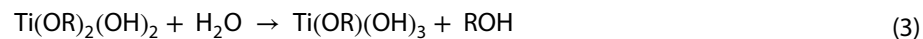
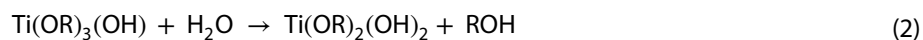
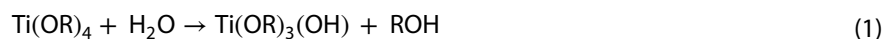
3.1 Role of beetroot extract in the synthesis

The precise identification of the secondary metabolites found in the beetroot used in this study has already been documented in works that are already reported in the literature. Beta vulgaris contains a variety of biologically active phytochemicals, such as betalains, flavonoids, polyphenols, saponins, and inorganic nitrate. It is also a rich source of a variety of minerals, including potassium, sodium, phosphorous, calcium, magnesium, copper, iron, zinc, and manganese [32–34]. Betanin (betanidin 5-O- β -D-glucoside, the major red beet pigment) is a betalains pigment and is used as a powerful antioxidant and coloring agent in the food industry. Due to its strong antioxidant and reducing activity, which is based on its capacity to capture free radicals, betanin may function as a reducing agent [35]. Additionally, betanin can act as a natural capping agent to stabilize metal/metal oxide nanoparticles because of its capacity to coordinate metal ions. The green synthesis of Ag/TiO₂ nanocomposites in the presence of beetroot extract has been reported [35], where Betanin was suggested to act both as a reducing and a capping agent.

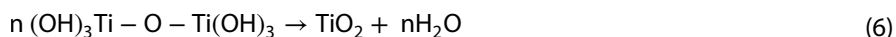
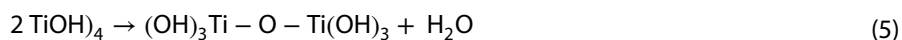
3.2 Reaction mechanism involved in the synthesis of TiO₂-NPs

The formation of TiO₂-NPs in the present study involves two steps: (i) hydrolysis and (ii) condensation. Titanium isopropoxide (Ti(C₃H₇O)₄), is used as the Ti⁴⁺ ion precursor, which usually undergoes hydrolysis in the presence of H₂O as reported in the previous studies. The mechanism for the formation of TiO₂-NPs is shown below [36]:

Hydrolysis



Condensation

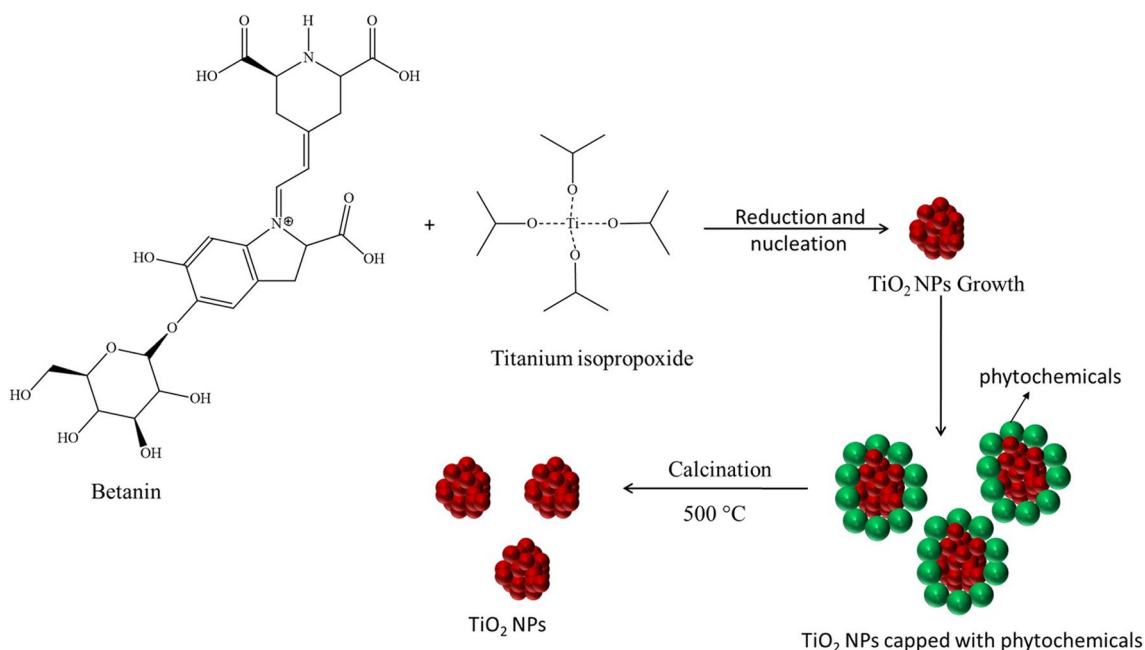


where R is the isopropyl group, titanium isopropoxide condenses to produce oxopolymers, which are then converted into a TiO_2 network in a series of stages.

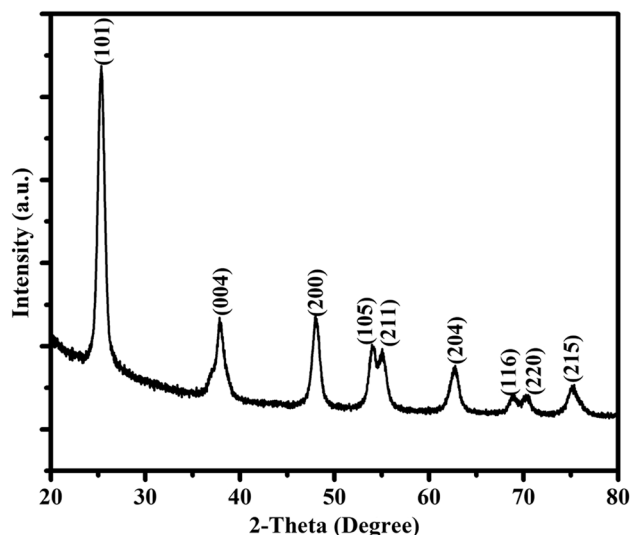
The type and concentration of phytochemicals found in the extract, along with the concentration of metal alkoxide precursor, are the key factors influencing the nanoparticle growth conditions, in the current study. The chemical interaction between the surface of TiO_2 -NPs and the phenolic $-\text{OH}$ present in the betanin may be responsible for controlling particle size and stability [36]. The proposed capping mechanism of betanin on the TiO_2 -NPs is shown in Scheme 1.

3.3 Characterization of TiO_2 -NPs

XRD pattern of the TiO_2 -NPs is shown in Fig. 1 and it indicates that the sample possesses an anatase phase and there are no peaks corresponding to the rutile phase. Intense reflections reveal the high crystallinity of the sample. The reflections at 2θ values of 25.28° , 37.85° , 48.04° , 54.17° , 55.13° , 62.68° , 68.98° , 70.18° , and 75.09° , correspond to (101), (004), (200), (105), (211), (204), (116), (220) and (215) crystal planes of the tetragonal phase (space group $I4_1/amd$) of TiO_2 [37–39] and it matches well with the pattern of the database (PDF 00-004-0477). Debye–Scherrer equation (Eq. 1) is used to calculate the crystallite size of the TiO_2 -NPs.



Scheme 1 The proposed capping mechanism of the betanin on TiO_2 -NPs

Fig. 1 XRD pattern of TiO₂-NPs

$$D = \frac{0.9\lambda}{\beta \cos \theta}$$

where λ represents the wavelength of the X-ray radiation (Cu K α = 0.15418 nm), θ represents the Bragg diffraction angle, β represents the full width at half-maximum height, and D represents the average crystallite size. The obtained crystallite size for TiO₂-NPs is 9.8 nm.

The Raman spectrum was used to further confirm the phase and purity of the synthesized TiO₂-NPs to provide a deeper understanding of the structure (Fig. 2). The trigonal anatase phase has a space group of I41/amd and its local symmetry is D2d [40]. The characteristic peaks centered at 142 (E_g), 195 (E_g), 393 (B_{1g}), 514 (A_{1g}), and 637 cm⁻¹ (E_g) demonstrate the anatase phase, without any band for rutile or brookite phase [41]. The band located at 637 cm⁻¹ (E_g) corresponds to the Ti–O stretching mode and the band that appeared at 397 cm⁻¹ (B_{1g}) refers to the O–Ti–O bending mode [42]. Thus, there is good agreement between the Raman spectrum and XRD data, confirming the existence of the high-purity TiO₂ anatase phase.

Figure 3 displays the FTIR spectrum of anatase TiO₂-NPs. The broad band centered at 500–600 cm⁻¹ corresponds to the Ti–O–Ti bending vibration in the TiO₂ structure. The broad band centered at 3600–3400 cm⁻¹ refers to the intermolecular

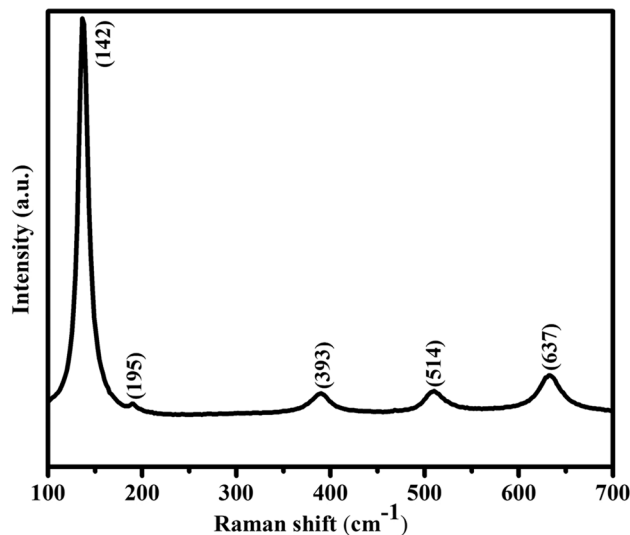
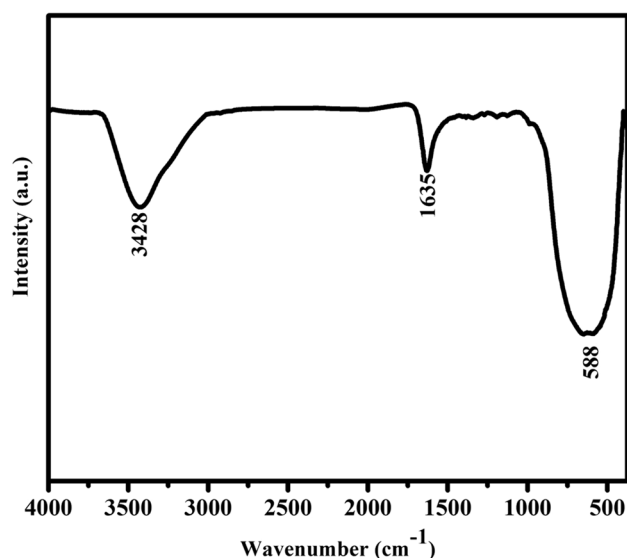
Fig. 2 Raman spectrum of the anatase TiO₂-NPs

Fig. 3 FTIR spectrum of the anatase TiO₂-NPs



interaction of the -OH groups in H₂O molecule present on TiO₂ surface. The band at 1635 cm⁻¹ refers to signature -OH bending vibration [43].

Figure 4a represents the N₂ adsorption–desorption isotherm of as-synthesized TiO₂-NPs and is used to measure the surface area. The results revealed that at the relative pressure P/P_0 of 0.99, the anatase TiO₂-NPs possess type IV isotherm with a hysteresis loop. The mesoporous nature of the TiO₂-NPs is suggested by the characteristic loop, and their presence can be attributed to the breakdown of biomolecules that have been capped on the surface of TiO₂ and the release of CO₂ during calcination. The adsorption isotherm curve is used to calculate the BET surface area of TiO₂-NPs and the obtained value is around 63.2 m²g⁻¹. The associated pore size distribution plot derived from the adsorption data using the Density Functional Theory (DFT) approach is shown in Fig. 4b. Results show that the sample has an average pore diameter of 5.43 nm and a pore volume of 0.257 cm³g⁻¹.

SEM analysis was used to investigate the surface morphology of TiO₂-NPs, as shown in Fig. 5. SEM images indicate that the particles are agglomerated into a spherical sponge-like bunch of particles. The irregular primary particles form a loose and porous structure that makes it easy for lithium-ion diffusion and electrolyte infiltration into the bulk phase. Moreover, the smaller particles enable faster Li⁺ ion insertion and de-insertion in the TiO₂ anode material, leading to improved charge and discharge process, especially at high C-rate cycling.

TEM was employed to examine the actual shape and size of TiO₂-NPs. The TEM image indicates that the synthesized TiO₂-NPs are spherical in shape. The TEM image further demonstrates that the biomolecules in the beta extract act as

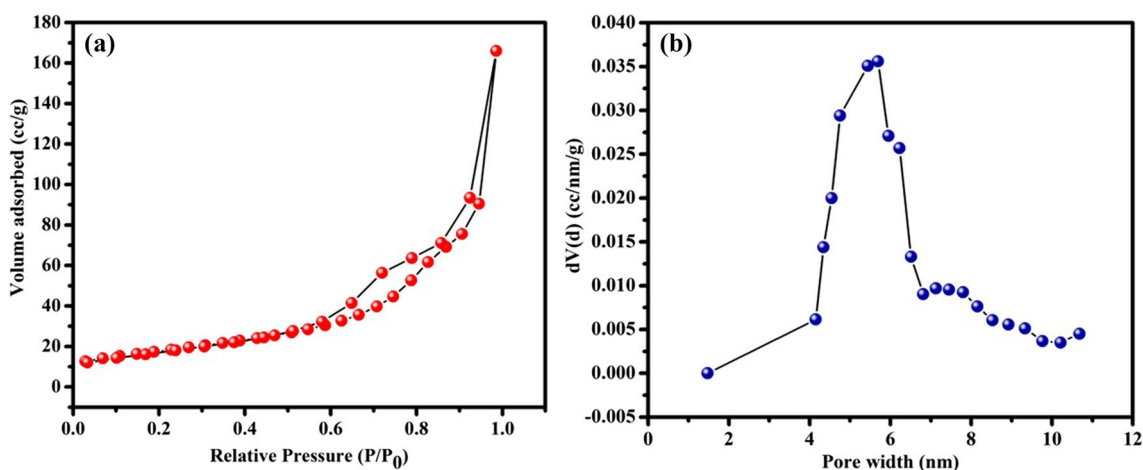


Fig. 4 **a** N₂ adsorption/desorption isotherms and **b** the pore size distribution of TiO₂-NPs

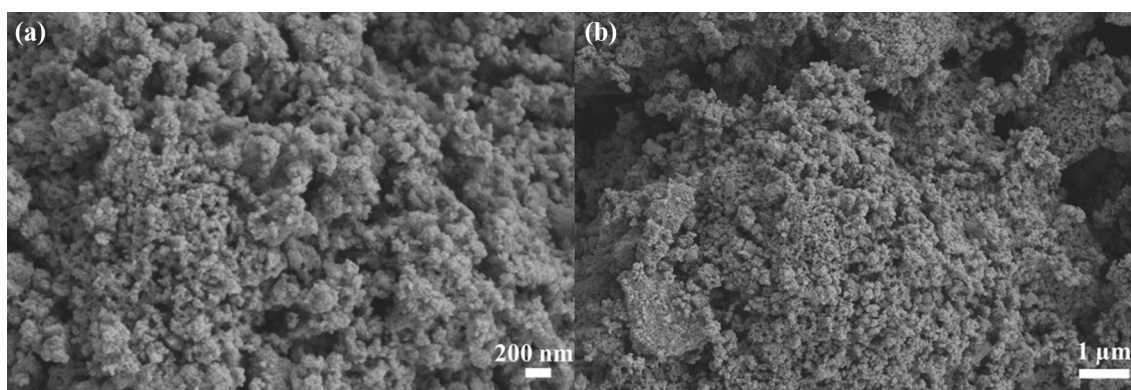


Fig. 5 SEM images of TiO₂-NPs at different magnifications, **a** at 25.0 kX and **b** at 10.0 kX

capping agents, preventing the severe aggregation of TiO₂-NPs. (Figs. 6a and b). The average particle size of each grain is 12 nm, which is comparable with the estimated crystallite size from XRD. The diffused rings in the selected area electron diffraction (SAED) pattern (Fig. 6c) indicate the polycrystalline nature of the synthesized TiO₂-NPs. Moreover, it confirms the findings from XRD and Raman studies that the final TiO₂ possesses an anatase phase. Furthermore, the SAED pattern strongly supports the XRD findings by showing the growth of nanoparticles along the (101), (004), and (200) planes. The HR-TEM images shown in Fig. 6d show lattice fringes with a d-spacing of 0.35 nm, corresponding to the (101) plane of highly crystalline tetragonal anatase TiO₂. The Fig. 6e represents the particle size histogram of TiO₂-NPs, which indicates that the average particle size is ~ 12 nm.

3.4 Electrochemical performance of TiO₂-NPs as anode material

The electrochemical performance of TiO₂-NPs was studied in CR2032 coin cells with Li metal as the counter electrode. At a scan rate of 100 μV s⁻¹, half-cells were first subjected to CV measurements in the voltage window of 0.5 to 3.5 V vs Li⁺/Li. Figure 7 shows the CV test results for the initial three cycles. To facilitate lithium-ion insertion into the TiO₂ crystal structure, the half-cell was initially discharged. Thus, a change in the valence state of titanium from Ti⁴⁺ to Ti³⁺ takes place. The Li-ion insertion (reduction peak) and extraction (oxidation peak), which occurred during the cathodic and anodic sweeps, respectively, are illustrated by the strong peaks at 1.72 and 2.12 V. In crystalline anatase electrodes, the separation of cathodic and anodic peaks is prevalent. These peaks show the exceptional reversibility of the anatase TiO₂-NPs as an insertion host because during discharging Ti⁴⁺ was converted to Ti³⁺ and then oxidized to Ti⁴⁺ during charging. Sharp cathodic/anodic peaks during electrochemical Li⁺ intercalation/de-intercalation demonstrate the two-phase reaction mechanism in accordance with the following reaction: TiO₂ + xLi⁺ + xe⁻ ↔ Li_xTiO₂ [44]. Nevertheless, a slight deviation in the peak position is seen in the succeeding cycles which may be due to the small stress developed in the TiO₂ lattice during Li⁺ insertion/extraction process.

The galvanostatic charge–discharge curves of TiO₂-NPs in the voltage window of 1.0–3.0 V (C/10 rate) are shown in Fig. 8. In the first step, the half-cell was discharged to intercalate Li⁺ ions into the TiO₂ lattice. Due to the loss of symmetry in the y direction during the lithium-ion intercalation, the unit cell symmetry of anatase undergoes a first-order phase transition from its initial tetragonal (I41/amd) structure to the orthorhombic (Pmn21) structure [30]. This phase transition happens simultaneously with a spontaneous phase separation of the lithium-poor (Li_{0.01}TiO₂) phase into the lithium-rich (Li_{0.69}TiO₂) phase, which was previously observed by several investigations [45, 46]. Though anatase TiO₂-NPs have a theoretical specific capacity of 335 mAh g⁻¹, the actual capacity that may be achieved is much lower due to the significant Li–Li repulsion in the Li_xTiO₂ framework at a higher degree of insertion, i.e., x > 0.5. In the present work, the anatase TiO₂-NPs delivered an initial discharge capacity of 209.7 mAh g⁻¹, which is equivalent to inserting 0.62 mol of lithium per formula unit. During the initial charging, the half-cell exhibited a capacity of 184 mAh g⁻¹ (0.55 mol lithium per formula unit). The irreversible capacity during the initial discharge–charge process is ~ 25.7 mAh g⁻¹ (corresponds to 0.076 mol Li), which is lower than other previously published works (Table 1). The charge–discharge curves show shortened plateaus at 1.78 V and 1.9 V. The plateau at 1.78 V refers to the Li-ion insertion (discharge) and the plateau at ~ 1.9 V refers to the Li-ion de-insertion (charge) [47]. The existence of a plateau region in the discharge–charge process demonstrates that the Li insertion occurs via a two-phase reaction mechanism and is in good agreement with CV peaks.

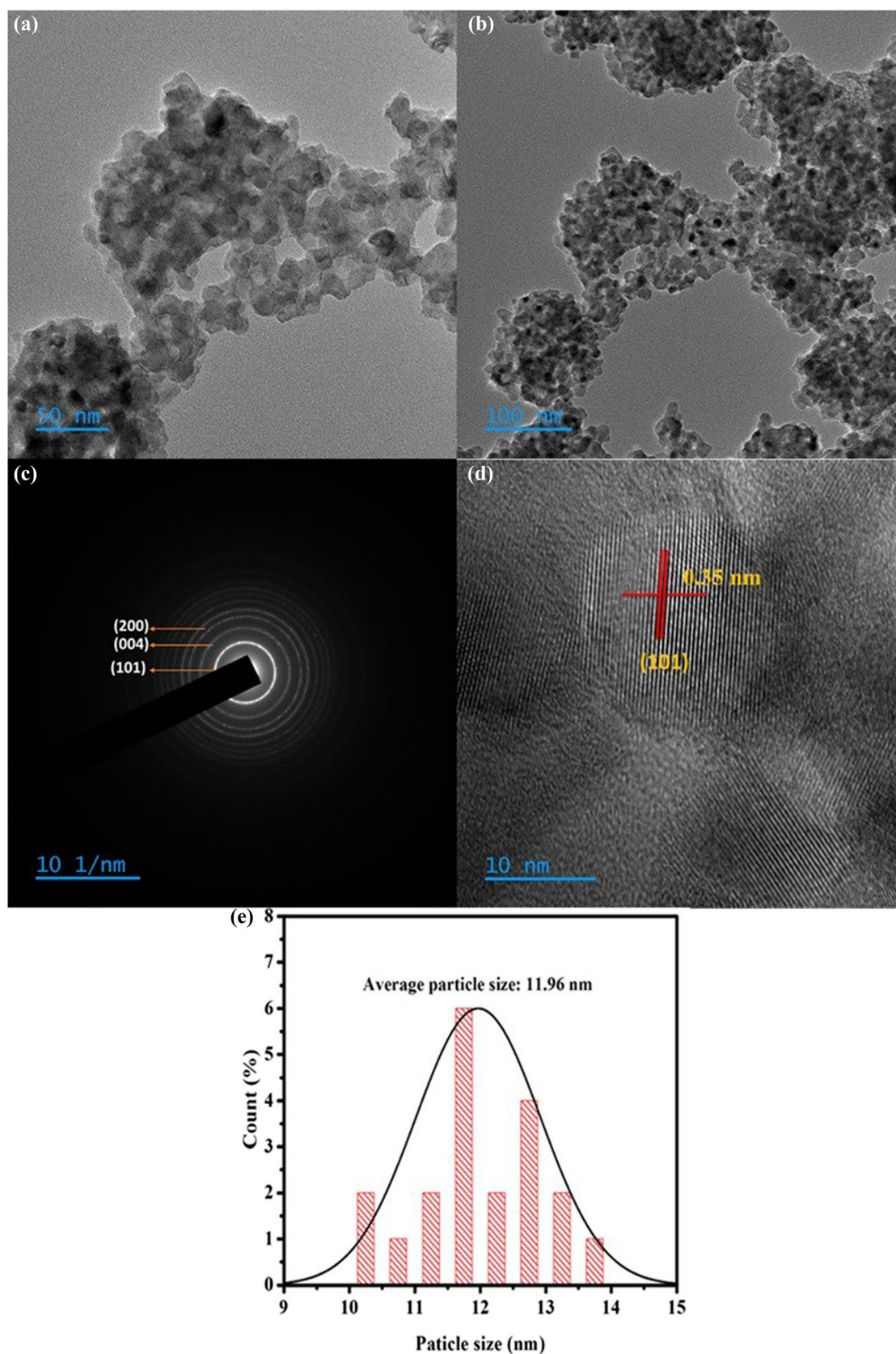


Fig. 6 **a,b** TEM images of TiO₂-NPs at different magnifications, **c** SAED pattern, **d** HR-TEM image of TiO₂-NPs, and **e** the particle size distribution histogram of TiO₂-NPs

Fig. 7 CV plots of TiO₂-NPs in the voltage window of 0.5–3.5 V at a scan rate of 100 $\mu\text{V s}^{-1}$

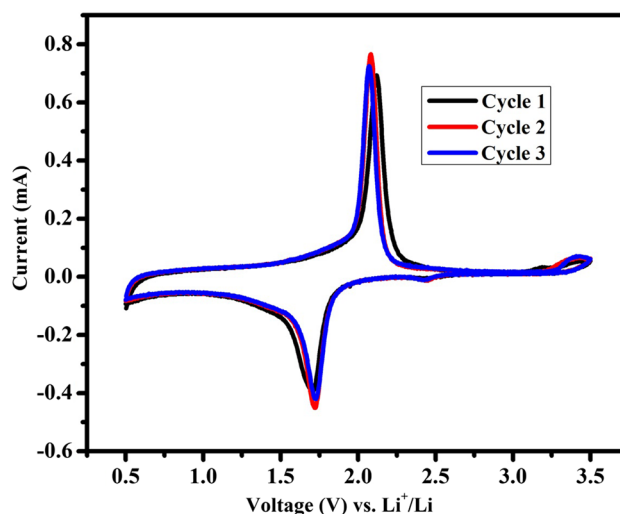
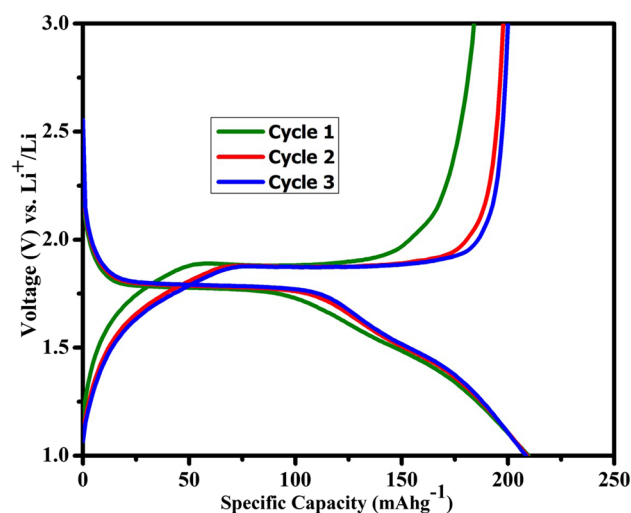


Fig. 8 The first three charge–discharge curves of anatase-TiO₂-NPs cycled at C/10 rate in the voltage window 1.0–3.0 V



The cycling performance and rate capability of anatase TiO₂-NPs are shown in Fig. 9. The rate capability study is employed to examine the stability and versatility of the Li/TiO₂ half-cell. Figure 9a shows the rate performance of Li/TiO₂ half-cells at different current rates. The cell delivered discharge capacities of about 209.7, 203, 200, 196, 192, 183, 173, and 149 mAh g^{-1} at various current densities of C/10, C/5, C/2, 1C, 2C, 5C, 10C, and 20C, respectively. Figure 9a indicates that as the rate capability tests are repeated and the electrode cycled back at a high C-rate (20C), the material still delivers a discharge capacity of 132 mAh g^{-1} . Thus, this gives evidence of the structural stability and electrochemical reversibility of the TiO₂-NPs sample. Figure 9b demonstrates the cyclability of Li/TiO₂ half-cell at three different current rates (1C, 2C, and 5C) for 100 cycles. The results revealed that the cell exhibited capacity retentions of 88.9% at 1C, 88.1% at 2C, and 81.2% at 5C rate at the end of 100 cycles. Figure 10 represents the coulombic efficiency of Li/TiO₂ half-cell during cycling, and rate performances and the results indicate that during both studies the coulombic efficiency is $\sim 100\%$. As compared with previously reported work, the present bio-mediated anatase TiO₂-NPs exhibited better cycling and rate performances (Table 1).

Cyclic voltammetry at various scan rates (100–900 $\mu\text{V s}^{-1}$) was used to investigate the lithium-ion diffusion coefficient, D_{Li} in TiO₂-NPs (Fig. 11a). As the scan rate increases, the reduction peaks shift toward lower voltage and the oxidation peaks gradually shift toward high voltage. Figure 11b depicts the relationship between the square root of the scan rate ($v^{1/2}$) and peak current (I_p). The diffusion coefficient was calculated by Randles Sevcik equation [48–50],

Table 1 A comparison of electrochemical performances of anatase TiO₂ samples prepared in this work with previously reported materials

Material	Potential window (V)	Initial discharge capacity in mAhg ⁻¹	Irreversible capacity during first discharge-charge process (mAhg ⁻¹)	Cycle life, Capacity in mAhg ⁻¹ (Rate and no of cycles is given in parenthesis)	Rate capability (Rate is given in parenthesis)	Reference
Bio-TiO ₂	1.0–3.0	230	24	164 (33 mA g ⁻¹ , 60)	46 (2 Ag ⁻¹)	Kashale et al. [51]
Anatase TiO ₂	1.0–3.0	221	32	182 (C/10, 30)	45 (30C)	El-Deen et al. [52]
Rutile and Anatase Composite TiO ₂ Nanotube (450 °C)	1.0–3.0	180	7	160 (C/10, 100)	62 (3C)	Wei et al. [53]
Rutile and Anatase Composite TiO ₂ Nanotube (600 °C)	1.0–3.0	230	20	185 (C/10, 100)	60 (3C)	Wei et al. [53]
TiO ₂ (B) nanosheets	1.0–3.0	245	84	162 (C/10, 25)	–	Wu et al. [54]
TiO ₂ -nanobelt	1.0–3.0	250	–	110 (C/10, 10)	–	Luo et al. [55]
TiO ₂ -230 °C	1.0–3.0	203.3	62.5	100 (0.12C, 10)	–	Luo et al. [56]
Lotus-root shaped TiO ₂	1.0–3.0	120	–	89 (0.5C, 100)	67 (2C)	Choi et al. [57]
Anatase TiO ₂ nanotubes	1.0–3.0	123	–	142 (36 mA g ⁻¹ , 100)	122 (144 mA g ⁻¹)	Fasakin et al. [58]
Porous anatase TiO ₂ -NPs	1.0–3.0	225	52	183 (5C, 20)	161 (10C)	Li et al. [59]
Anatase TiO ₂ -NPs	1.0–3.0	209.7	25.7	148.7 (5C, 100)	149.5 (20C)	This work

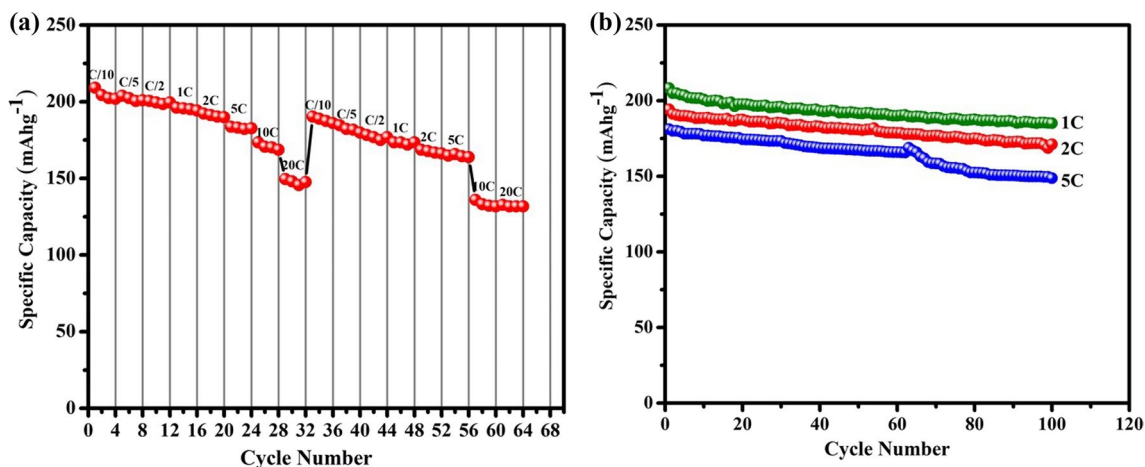


Fig. 9 **a** Rate capability, and **b** cyclability profiles of the Li/TiO₂ half-cell

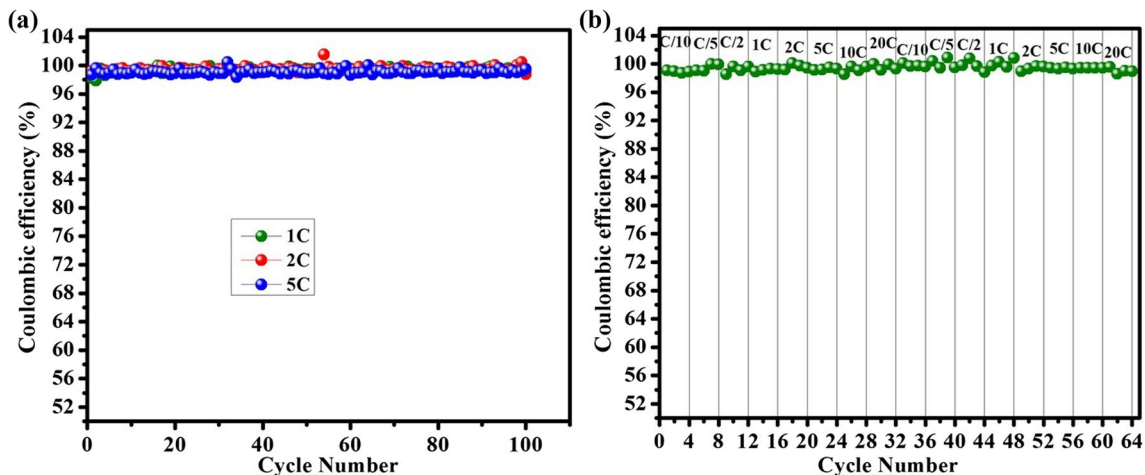


Fig. 10 Coulombic efficiency of Li/TiO₂ half-cell during **a** cycling, and **b** rate performance

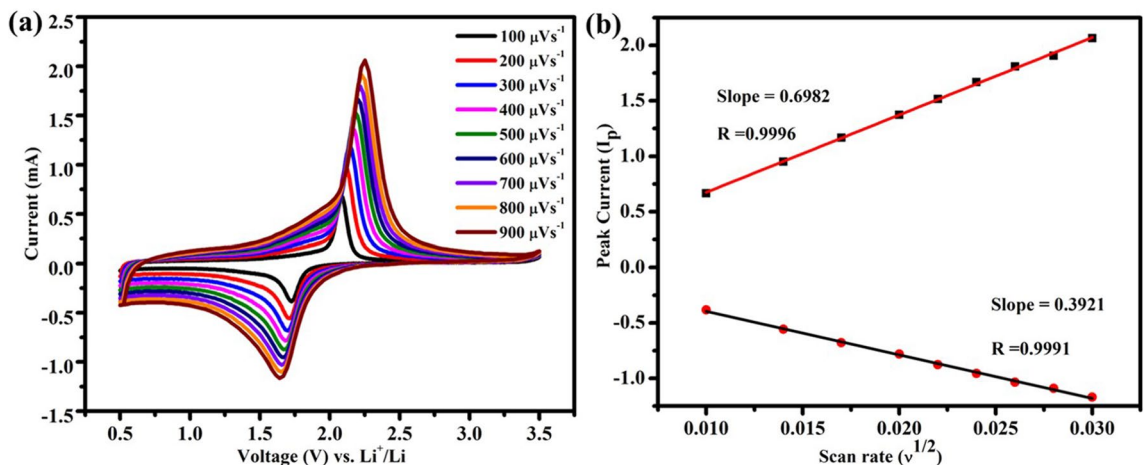


Fig. 11 **a** CV curves of Li/TiO₂ half-cell at different scan rates (from 100 μVs⁻¹ to 900 μVs⁻¹) and, **b** the plot of $u^{1/2}$ vs. I_p

$$I_p = 2.69 \times 10^5 n^{3/2} A D^{1/2} C_{Li} v^{1/2}$$

where n is the number of electrons transferred, A is the surface area of the electrode, D is the lithium-ion diffusion coefficient, C_{Li} is the concentration of Li^+ ion in the electrode, v is the scan rate and I_p is the peak current. The diffusion coefficient of Li^+ -ions calculated based on both anodic and cathodic peaks for the TiO_2 -NPs is $5.72 \times 10^{-11} \text{ cm}^2\text{s}^{-1}$ and $1.86 \times 10^{-10} \text{ cm}^2\text{s}^{-1}$ for de-lithiation and lithiation processes, respectively. Thus, the higher diffusion coefficient is responsible for the superior rate and cycling performance of the present anatase TiO_2 -NPs.

4 Conclusions

In summary, anatase TiO_2 -NPs were successfully synthesized through a green-mediated process using Beta vulgaris (Beetroot) extract. The material was characterized by X-ray diffraction (XRD), Raman spectroscopy, infra-red (IR) spectroscopy, scanning electron microscopy (SEM), transmission electron microscopy (TEM) analysis, and evaluated as anode in lithium-ion cells. Furthermore, an aqueous binder (a combination of CMC and SBR) is employed for electrode processing. The electrochemical performance of the Li/TiO_2 half-cell was evaluated in the potential window of 1–3 V at C/10 rate. The cycling stability and rate capability studies demonstrate that the material exhibits superior performances than the previously reported TiO_2 -NPs material. Even at 20 C rate, the material delivered a discharge capacity of 149 mAhg^{-1} . Hence, the present work highlights a completely greener approach for both material synthesis and electrode processing. This work will be highly beneficial for producing anodes for high-power LIBs in a cost-effective and environmentally friendly route.

Acknowledgements We acknowledge the Director, Vikram Sarabhai Space Centre, Thiruvananthapuram for granting permission to publish this paper. The authors also thank the Analytical and Spectroscopy Division, Vikram Sarabhai Space Centre for providing facilities for characterization. Akhilash M is thankful to the University of Kerala for availing fellowship (Junior Research Fellowship, University of Kerala Registration No. AcEVI(2)/718/CHE/18145/2018).

Author contributions A M P: Conceptualization, Design, Methodology, Formal analysis, Investigation, Visualization, Writing-Original Draft, Writing-review/editing S V G: Conceptualization, Methodology, Formal analysis, Investigation P V R L P: Conceptualization, Methodology, Formal analysis, Investigation P S S: Conceptualization, Methodology, Formal analysis, Investigation B J: Conceptualization, Methodology, Investigation, Writing - Review & Editing, Visualization, Supervision S S A: Supervision, Project administration M T D: Supervision, Project administration.

Data availability All data generated or analyzed during this study are included in this published article.

Declarations

Competing interests The authors declare no competing interests.

Open Access This article is licensed under a Creative Commons Attribution 4.0 International License, which permits use, sharing, adaptation, distribution and reproduction in any medium or format, as long as you give appropriate credit to the original author(s) and the source, provide a link to the Creative Commons licence, and indicate if changes were made. The images or other third party material in this article are included in the article's Creative Commons licence, unless indicated otherwise in a credit line to the material. If material is not included in the article's Creative Commons licence and your intended use is not permitted by statutory regulation or exceeds the permitted use, you will need to obtain permission directly from the copyright holder. To view a copy of this licence, visit <http://creativecommons.org/licenses/by/4.0/>.

References

1. Han B, Kim SJ, Hwang BM, Kim SB, Park KW. Single-crystalline rutile TiO_2 nanowires for improved lithium ion intercalation properties. *J Power Sources*. 2013;222:225–9. <https://doi.org/10.1016/j.jpowsour.2012.08.073>.
2. Akhilash M, Salini PS, Bibin J, Sujatha S, Mercy TD. Transition metal based cathode materials for lithium-ion cells. In Veronica J. Avila, editors *Transition metals—an overview*. Nova Publisher 2023; 142.
3. Zhao S, Sun B, Yan K, Zhang J, Wang C, Wang G. Aegis of lithium-rich cathode materials via heterostructured $LiAlF_4$ coating for high-performance lithium-ion batteries. *ACS Appl Mater Interfaces*. 2018;10(39):33260–8. <https://doi.org/10.1021/acsami.8b11471>.
4. Pillai AM, Salini PS, John B, Devassy MT. Aqueous binders for cathodes: a lodestar for greener lithium ion cells. *Energy Fuels*. 2022;36(10):5063–87. <https://doi.org/10.1021/acs.energyfuels.2c00346>.
5. Chen Y, Zhang Y, Chen B, Wang Z, Lu C. An approach to application for $LiNi_{0.6}Co_{0.2}Mn_{0.2}O_2$ cathode material at high cutoff voltage by TiO_2 coating. *J Power Sour*. 2014;256:20–7. <https://doi.org/10.1016/j.jpowsour.2014.01.061>.

6. Akhilash M, Salini PS, Jalaja K, John B, Mercy TD. Synthesis of $\text{Li}_{1.5}\text{Ni}_{0.25}\text{Mn}_{0.75}\text{O}_{2.5}$ cathode material via carbonate co-precipitation method and its electrochemical properties. *Inorgan Chem Commun.* 2021;126:108434. <https://doi.org/10.1016/j.inoche.2020.108434>.
7. Akhilash M, Salini PS, John B, Sujatha S, Mercy TD. Surface modification on nickel rich cathode materials for lithium-ion cells: a mini review. *Chem Rec.* 2023;23(11): e202300132. <https://doi.org/10.1002/tcr.202300132>.
8. Cabello M, Gucciardi E, Liendo G, Caizán-Juananera L, Carriazo D, Villaverde AA. Study to explore the suitability of $\text{LiNi}_{0.8}\text{Co}_{0.15}\text{Al}_{0.05}\text{O}_2/\text{silicon@graphite}$ cells for high-power lithium-ion batteries. *Int J Mol Sci.* 2021;22(19):10331. <https://doi.org/10.3390/ijms221910331>.
9. Akhilash M, Salini PS, John B, Mercy TD. A journey through layered cathode materials for lithium ion cells—from lithium cobalt oxide to lithium-rich transition metal oxides. *J Alloy Compd.* 2021;869: 159239. <https://doi.org/10.1016/j.jallcom.2021.159239>.
10. Park JS, Mane AU, Elam JW, Croy JR. Amorphous metal fluoride passivation coatings prepared by atomic layer deposition on LiCoO_2 for Li-ion batteries. *Chem Mater.* 2015;27(6):1917–20. <https://doi.org/10.1021/acs.chemmater.5b00603>.
11. Akhilash M, Salini PS, John B, Mercy TD. The renaissance of high-capacity cathode materials for lithium ion cells. *Energy Harves. Storage* 2022; 181–208. https://doi.org/10.1007/978-981-19-4526-7_6
12. Angelopoulou P, Paloukis F, Słowik G, Wójcik G, Avgouropoulos G. Combustion-synthesized $\text{Li}_x\text{Mn}_2\text{O}_4$ -based spinel nanorods as cathode materials for lithium-ion batteries. *Chem Eng J.* 2017;311:191–202. <https://doi.org/10.1016/j.cej.2016.11.082>.
13. Pillai AM, Salini PS, John B, Nair VS, Jalaja K, Sarojiniamma S, Devassy MT. Cobalt-free Li-rich high-capacity cathode material for lithium-ion cells synthesized through sol-gel method and its electrochemical performance. *Ionics.* 2022;28(11):5005–14. <https://doi.org/10.1007/s11581-022-04725-x>.
14. Akhilash M, Salini PS, John B, Supriya N, Sujatha S, Mercy TD. Thermal stability as well as electrochemical performance of Li-rich and Ni-rich cathode materials—a comparative study. *Ionics.* 2023. <https://doi.org/10.1007/s11581-022-04873-0>.
15. Pupurs A, Varna J. Modeling mechanical stress and exfoliation damage in carbon fiber electrodes subjected to cyclic intercalation/deintercalation of lithium ions. *Compos B Eng.* 2014;65:69–79. <https://doi.org/10.1016/j.compositesb.2013.11.007>.
16. Prakash AS, Manikandan P, Ramesha K, Sathiyam M, Tarascon JM, Shukla AK. Solution-combustion synthesized nanocrystalline $\text{Li}_4\text{Ti}_5\text{O}_{12}$ as high-rate performance Li-ion battery anode. *Chem Mater.* 2010;22(9):2857–63. <https://doi.org/10.1021/cm100071z>.
17. Ma XH, Zeng SS, Zou BK, Liang X, Liao JY, Chen CH. Synthesis of different CuO nanostructures by a new catalytic template method as anode materials for lithium-ion batteries. *RSC Adv.* 2015;5(71):57300–8. <https://doi.org/10.1039/C5RA10825J>.
18. Weng Z, Guo H, Liu X, Wu S, Yeung KWK, Chu PK. Nanostructured TiO_2 for energy conversion and storage. *RSC Adv.* 2013;3(47):24758–75. <https://doi.org/10.1039/C3RA44031A>.
19. Kang JW, Kim DH, Mathew V, Lim JS, Gim JH, Kim J. Particle size effect of anatase TiO_2 nanocrystals for lithium-ion batteries. *J Electrochem Soc.* 2010;158(2):A59. <https://doi.org/10.1149/1.3518420>.
20. Pillai AM, Salini PS, John B, Suchithra C, Sarojiniamma S, Devassy MT. Lithium-rich $\text{Li}_{1.17}\text{Ni}_{0.17}\text{Co}_{0.17}\text{Mn}_{0.5}\text{O}_2$ cathode material for lithium-ion cells: effect of calcination temperature on electrochemical performance. *Energy Fuels.* 2023;37(18):14334–40. <https://doi.org/10.1021/acs.energyfuels.3c02174>.
21. Zhang Y, Meng Y, Zhu K, Qiu H, Ju Y, Gao Y, Du F, Zou B, Chen G, Wei Y. Copper-doped titanium dioxide bronze nanowires with superior high rate capability for lithium ion batteries. *ACS Appl Mater Interfaces.* 2016;8(12):7957–65. <https://doi.org/10.1021/acsami.5b10766>.
22. Lan T, Zhang W, Wu NL, Wei M. Nb-doped rutile TiO_2 mesocrystals with enhanced lithium storage properties for lithium ion battery. *Chem Eur J.* 2017;23(21):5059–65. <https://doi.org/10.1002/chem.201605115>.
23. Han H, Song T, Bae J-Y, Nazar LF, Kim H, Paik U. Nitridated TiO_2 hollow nanofibers as an anode material for high power lithium ion batteries. *Energy Environ Sci.* 2011;4(11):4532–6. <https://doi.org/10.1039/C1EE02333K>.
24. Niu RL, Sheng ZM, Xu QM, Chang CK, Huang YS, Han S. Small anatase TiO_2 nanoparticles grown on carbon nanocages as anodes for high performance sodium and lithium ion batteries. *Chem Phys Lett.* 2022;790: 139350. <https://doi.org/10.1016/j.cplett.2022.139350>.
25. Choi MG, Lee YG, Song SW, Kim KM. Lithium-ion battery anode properties of TiO_2 nanotubes prepared by the hydrothermal synthesis of mixed (Anatase and Rutile) particles. *Electrochim Acta.* 2010;55(20):5975–83. <https://doi.org/10.1016/j.electacta.2010.05.052>.
26. Subramanian V, Karki A, Gnanasekar KI, Eddy FP, Rambabu B. Nanocrystalline TiO_2 (Anatase) for Li-ion batteries. *J Power Sour.* 2006;159(1):186–92. <https://doi.org/10.1016/j.jpowsour.2006.04.027>.
27. Arabatzis IM, Falaras P. Synthesis of porous nanocrystalline TiO_2 foam. *Nano Lett.* 2003;3(2):249–51. <https://doi.org/10.1021/nl0259028>.
28. Chae SY, Park MK, Lee SK, Kim TY, Kim SK, Lee WI. Preparation of size-controlled TiO_2 nanoparticles and derivation of optically transparent photocatalytic films. *Chem Mater.* 2003;15(17):3326–31. <https://doi.org/10.1021/cm030171d>.
29. Guler MO, Cevher O, Cetinkaya T, Tocoglu U, Akbulut H. High capacity TiO_2 anode materials for Li-ion batteries. *Energy Convers Manage.* 2013;72:111–6. <https://doi.org/10.1016/j.enconman.2012.11.026>.
30. Zhang X, Suresh Kumar P, Aravindan V, Liu HH, Sundaramurthy J, Mhaisalkar SG, Duong HM, Ramakrishna S, Madhavi S. Electrospun TiO_2 -graphene composite nanofibers as a highly durable insertion anode for lithium ion batteries. *J Phys Chem C.* 2012;116(28):14780–8. <https://doi.org/10.1021/jp302574g>.
31. Akhilash MS, Salini P, John B, Sujatha SD, Mercy T. A comparative study of aqueous- and non-aqueous-processed Li-rich $\text{Li}_{1.5}\text{Ni}_{0.25}\text{Mn}_{0.75}\text{O}_{2.5}$ cathodes for advanced lithium-ion cells. *RSC Sustainability.* 2024;2(2):416–24. <https://doi.org/10.1039/D3SU00168G>.
32. Mirmiran P, Houshialsadat Z, Gaeini Z, Bahadoran Z, Azizi F. Functional properties of beetroot (Beta Vulgaris) in management of cardio-metabolic diseases. *Nutr Metab.* 2020;17(1):3. <https://doi.org/10.1186/s12986-019-0421-0>.
33. Kosa SA, Zaheer Z. Betanin assisted synthesis of Betanin@silver nanoparticles and their enhanced adsorption and biological activities. *Food Chem.* 2019;298: 125014. <https://doi.org/10.1016/j.foodchem.2019.125014>.
34. Pillai AM, Sivasankarapillai VS, Rahdar A, Joseph J, Sadeghfar F, Anuf AR, Rajesh K, Kyzas GZ. Green synthesis and characterization of zinc oxide nanoparticles with antibacterial and antifungal activity. *J Mol Struct.* 1211, 128107 (2020). <https://doi.org/10.1016/j.molstruc.2020.128107>.
35. Jayapriya M, Arulmozhi M. Beta vulgaris peel extract mediated synthesis of Ag/TiO_2 nanocomposite: characterization, evaluation of antibacterial and catalytic degradation of textile dyes—an electron relay effect. *Inorgan Chem Commun.* 2021;128: 108529. <https://doi.org/10.1016/j.inoche.2021.108529>.

36. Rodríguez-Jiménez RA, Panecatí-Bernal Y, Carrillo-López J, Méndez-Rojas MÁ, Romero-López A, Pacio-Castillo M, Vivaldo I, Morales-Sánchez A, Arce RD, Caram J, Villanueva-Cab J, Alvarado J. Influence of ethanolic plant extracts on morphology and size distribution of sol-gel prepared TiO₂ nanoparticles. *ChemistrySelect*. 2021;6(16):3958–68. <https://doi.org/10.1002/slct.202100494>.
37. Oh SW, Park SH, Sun YK. Hydrothermal synthesis of nano-sized anatase TiO₂ powders for lithium secondary anode materials. *J Power Sources*. 2006;161(2):1314–8. <https://doi.org/10.1016/j.jpowsour.2006.05.050>.
38. Dong L, Li M, Dong L, Zhao M, Feng J, Han Y, Deng J, Li X, Li D, Sun X. Hydrothermal synthesis of mixed crystal phases TiO₂-reduced graphene oxide nanocomposites with small particle size for lithium ion batteries. *Int J Hydrogen Energy*. 2014;39(28):16116–22. <https://doi.org/10.1016/j.ijhydene.2014.01.029>.
39. Pillai AM, Salini PS, Rekha Krishnan G, Chithra A, John B, Pillai S, Sarojiniamma S, Devassy MT. Surface engineering of Li_{1.5}Ni_{0.25}Mn_{0.75}O_{2.5} cathode material using TiO₂ nanoparticles: an approach to improve electrochemical performance and thermal stability. *J Alloys Compounds*. 2024;976:173064. <https://doi.org/10.1016/j.jallcom.2023.173064>.
40. Gao K. Strongly intrinsic anharmonicity in the low-frequency raman mode in nanocrystalline anatase TiO₂. *Physica B*. 2007;398(1):33–7. <https://doi.org/10.1016/j.physb.2007.04.013>.
41. Ohsaka T, Izumi F, Fujiki Y. Raman spectrum of anatase, TiO₂. *J Raman Spectrosc*. 1978;7(6):321–4. <https://doi.org/10.1002/jrs.1250070606>.
42. Li F, Gu Y. Improvement of performance of dye-sensitized solar cells by doping Er₂O₃ into TiO₂ electrodes. *Mater Sci Semicond Process*. 2012;15(1):11–4. <https://doi.org/10.1016/j.mssp.2011.04.008>.
43. Al-Taweel SS, Saud HR. New route for synthesis of pure anatase TiO₂ nanoparticles via ultrasoundassisted sol-gel method. *J Chem Pharm Res* 2016; 8(2)
44. Exnar I, Kavan L, Huang SY, Grätzel M. Novel 2 V rocking-chair lithium battery based on nano-crystalline titanium dioxide. *J Power Sources*. 1997;68(2):720–2. [https://doi.org/10.1016/S0378-7753\(96\)02581-5](https://doi.org/10.1016/S0378-7753(96)02581-5).
45. Yang Z, Choi D, Kerisit S, Rosso KM, Wang D, Zhang J, Graff G, Liu J. Nanostructures and lithium electrochemical reactivity of lithium titanates and titanium oxides: a review. *J Power Sources*. 2009;192(2):588–98. <https://doi.org/10.1016/j.jpowsour.2009.02.038>.
46. Cava RJ, Murphy DW, Zahurak S, Santoro A, Roth RS. The crystal structures of the lithium-inserted metal oxides Li_{0.5}TiO₂ anatase, LiTi₂O₄ Spinel, and Li₂Ti₂O₄. *J Solid State Chem*. 1984;53(1):64–75. [https://doi.org/10.1016/0022-4596\(84\)90228-7](https://doi.org/10.1016/0022-4596(84)90228-7).
47. Shin JY, Samuelis D, Maier J. Sustained lithium-storage performance of hierarchical, nanoporous anatase TiO₂ at high rates: emphasis on interfacial storage phenomena. *Adv Func Mater*. 2011;21(18):3464–72. <https://doi.org/10.1002/adfm.201002527>.
48. Mohanan Pillai A, Salini PS, John B, Sarojiniamma S, Thelakkattu Devassy M. Synthesis and electrochemical characterization of a Li-rich Li_{1.17}Ni_{0.34}Mn_{0.5}O₂ cathode material for lithium-ion cells. *Energy Fuels*. 2022;36(18):11186–93. <https://doi.org/10.1021/acs.energyfuels.2c01231>.
49. Longo RC, Liang C, Kong F, Cho K. Core-shell nanocomposites for improving the structural stability of Li-rich layered oxide cathode materials for Li-ion batteries. *ACS Appl Mater Interfaces*. 2018;10(22):19226–34. <https://doi.org/10.1021/acsami.8b03898>.
50. Pillai AM, Salini PS, John B, Pillai S, Sarojiniamma S, Mercy T. Synthesis and characterization of Li_{1.25}Ni_{0.25}Mn_{0.5}O₂: a high-capacity cathode material with improved thermal stability and rate capability for lithium-ion cells. *J Alloys Compounds*. 2023;938:168363. <https://doi.org/10.1016/j.jallcom.2022.168363>.
51. Kashale AA, Gattu KP, Ghule K, Ingole VH, Dhanayat S, Sharma R, Chang JY, Ghule AV. Biomediated green synthesis of TiO₂ nanoparticles for lithium ion battery application. *Compos B Eng*. 2016;99:297–304. <https://doi.org/10.1016/j.compositesb.2016.06.015>.
52. El-Deen SS, Hashem AM, Abdel Ghany AE, Indris S, Ehrenberg H, Mauger A, Julien CM. Anatase TiO₂ nanoparticles for lithium-ion batteries. *Ionics*. 2018;24(10):2925–34. <https://doi.org/10.1007/s11581-017-2425-y>.
53. Wei J, Liu JX, Wu ZY, Zhan ZL, Shi J, Xu K. Research on the electrochemical performance of rutile and anatase composite TiO₂ nanotube arrays in lithium-ion batteries. *J Nanosci Nanotechnol*. 2015;15(7):5013–9. <https://doi.org/10.1166/jnn.2015.9847>.
54. Wu HY, Hon MH, Kuan CY, Leu IC. Preparation of TiO₂(B) nanosheets by a hydrothermal process and their application as an anode for lithium-ion batteries. *J Electron Mater*. 2014;43(4):1048–54. <https://doi.org/10.1007/s11664-013-2951-y>.
55. Luo W, Blanchard J, Xue Y, Taleb A. The influence of TiO₂ nanoparticles morphologies on the performance of lithium-ion batteries. *Nano-materials*. 2023;13(19):2636. <https://doi.org/10.3390/nano13192636>.
56. Luo W, Blanchard J, Tonelli D, Taleb A. Synthesis of TiO₂ nanobelt bundles decorated with TiO₂ nanoparticles and aggregates and their use as anode materials for lithium-ion batteries. *Micromachines*. 2023;14(2):243. <https://doi.org/10.3390/mi14020243>.
57. Choi SI, Jung EJ, Park M, Shin H-S, Huh S, Won YS. Phase-dependent performance of lotus-root shaped TiO₂ anode for lithium-ion batteries (LIBs). *Appl Surf Sci*. 2020;508:145237. <https://doi.org/10.1016/j.apsusc.2019.145237>.
58. Fasakin O, Oyedotun KO, Kebede M, Rohwer M, Roux LL, Mathe M, Eleruja MA, Ajayi EOB, Manyala N. Preparation and physico-chemical investigation of anatase TiO₂ nanotubes for a stable anode of lithium-ion battery. *Energy Rep*. 2020;6:92–101. <https://doi.org/10.1016/j.egy.2020.02.010>.
59. Li X, Zhang F, Zhai B, Wang X, Zhao J, Wang Z. Facile synthesis of porous anatase TiO₂ nanomaterials with the assistance of biomass resource for lithium ion batteries with high-rate performance. *J Phys Chem Solids*. 2020;145: 109552. <https://doi.org/10.1016/j.jpjcs.2020.109552>.